ChemPhysMater 3 (2024) 83–93

Contents lists available at ScienceDirect

ChemPhysMater

journal homepage: https://www.keaipublishing.com/en/journals/chemphysmater/

Research Article

Study of ZnO nanoparticle-supported clay minerals for electrochemical sensors, photocatalysis, and antioxidant applications

Mylarappa M[a,*], N. Raghavendra[b,*], N.R. Bhumika[c], C.H. Chaithra[c], B.N. Nagalaxmi[c], K.N. Shravana Kumara[c]

[a] Department of Chemistry, Sri Jagadguru Renukacharya College of Science, Arts & Commerce, Bengaluru 560009, India
[b] Department of Chemistry, East West Institute of Technology, Bengaluru 560091, India
[c] Department of Chemistry, Maharani Lakshmi Ammanni College for Women, Bengaluru 560012, India

ARTICLE INFO

Keywords:
Clay
Clay/ZnO
Photocatalytic
Electrochemical sensors

ABSTRACT

In view of the current study's demonstration of the synthesis of clay-doped ZnO composites, we present a low-cost method for producing clay-metal oxide (clay/ZnO). Utilizing the solution combustion technique, a composite of clay/ZnO was produced utilizing citric acid as both a fuel and a complexing agent. The hexagonal unit cell structure of the created clay/ZnO may be seen using XRD patterns. The ZnO-infused clay was visible in FE-SEM micrographs as homogenous, sphere-shaped ZnO. The possible involvement of clay/ZnO photocatalytic activity in the UV-induced photodegradation of malachite green dye was investigated. The 90% degradation rate shows the composite's outstanding photocatalytic degradation capacity. The resulting substance was electrochemically analyzed using a constructed electrode in 0.1 M KOH electrolyte. It increased its sensor capabilities, which now include chemical and biomolecule sensors, and it excelled in cyclic voltammetry-based redox potential studies. To efficiently evaluate chemically synthesized NPs for electrochemical, sensing, and photocatalytic applications, this study intends to create a solution combustion procedure for the synthesis of clay/ZnO nanocomposite using urea as fuel.

1. Introduction

Nanostructured materials have gained significant interest in recent years due to their unique properties, including enhanced damping, mechanical stability, high strength, and higher thermal conductivity [1]. Metal oxide nanostructures, characterized by their high surface area and tiny crystallite size, have found applications in optical electronics, sensing technologies, and nanoelectronics [2]. Various metal oxide nanostructures, such as Fe_3O_4, ZnO, TiO_2, and MgO, have been developed for a wide range of applications [3–6]. ZnO stands out as a sensor and device material due to its biosafety and biocompatibility. Metal oxide nanostructures possess desirable nano-morphological, functional, biocompatible, nontoxic, and catalytic properties [7]. These nano powders are in high demand in various industries and have received favorable market reception. ZnO nanoparticles and nanocomposite materials have been extensively researched due to their diverse applications in cutting-edge techniques [8,9]. Zinc oxide nano powders find applications in LCDs, solar cells, blue laser diodes, capacitors, protective coatings, photo printing, antimicrobial thin films, and electrophotography, among others [6].

Clay minerals serve as crucial adsorbents for removing harmful metals from water. Various methods [10,11] are available for producing nanocrystalline ferrites. The high surface area of these materials enhances their thermal and chemical stability, as well as their catalytic performance and cation exchangeability [12–14]. Layer-structured structural clay, known for its unique properties, is used to enhance sensor qualities during preparation [15,16]. Numerous studies [17–22] employing voltammetry have demonstrated the utility of clay-treated electrodes in detecting metals in water and bioactive chemicals. Among the available synthesis methods, co-precipitation [23–32] is the most effective for producing clay/ZnO nanocomposites.

Solution combustion is recommended for the production of ferrite nanoparticles [32] due to its convenience, rapid reaction, and low annealing temperature. This method results in improved physical properties, smaller particle sizes, and reduced impurities in the ferrites. Fuels are crucial in the combustion process as they facilitate the formation of metal cation molecules [33]. The low annealing temperature, short reaction time, and user-friendly nature of this method make it preferable to others [34]. Fuels such as glycine, urea, citric acid, and EDTA play a

* Corresponding authors.
E-mail addresses: mylu4mkallihatti@gmail.com (M. M), nraghavendra09@gmail.com (N. Raghavendra).

https://doi.org/10.1016/j.chphma.2023.07.002
Received 9 December 2022; Received in revised form 31 May 2023; Accepted 5 July 2023
Available online 9 August 2023

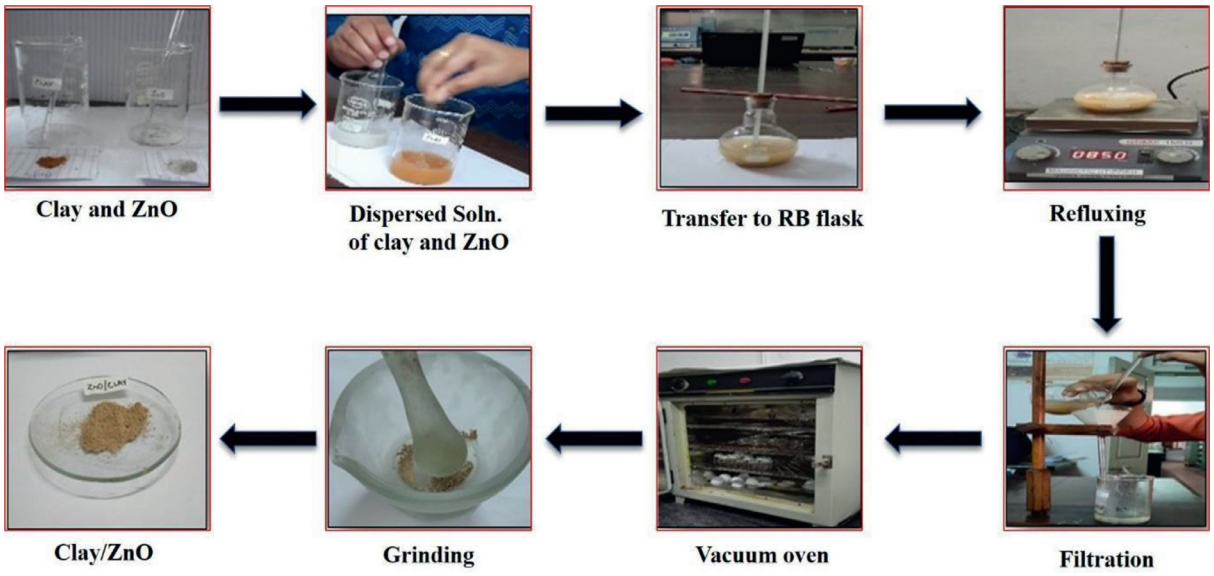

Fig. 1. Flowchart for synthesis of clay doped ZnO by reflux method.

significant role in the combustion reaction by forming complexes with metal cations [35,36].

Clay minerals, known for their high capacity to adsorb metal ions [37,38], are suitable adsorbents for various applications. They offer numerous benefits, including their effectiveness in detecting heavy metal particles in aqueous solutions that have been present for extended periods [39,40]. This study aims to establish a solution combustion approach using urea as a fuel for producing clay/ZnO nanocomposites. This method will provide an efficient means of evaluating chemically synthesized NPs for applications in electrochemical chemistry, sensor technology, and photocatalysis.

2. Materials and methods

2.1. Preparation of ZnO nanoparticles by solution combustion method

In a Pyrex dish, 15.368 g of $Zn(NO_3)_3$ and 6.0 g of urea were dissolved in double-distilled water. The dish was then placed inside a muffle furnace preheated to 400 °C. As the temperature increased, the solution reached its boiling point, causing dehydration and decomposition, resulting in the release of gasses. Once the solution reached its critical temperature, spontaneous combustion occurred, generating a significant amount of heat. The liquid completely evaporated, leaving behind a solid residue. Within 5 min, the combustion process resulted in the formation of ZnO powder.

2.2. Collection of clay

The clay used in the experiment was collected from the Kudremukh district of Karnataka. It was used without undergoing any additional purification or modification.

2.3. Preparation of clay doped ZnO nanocomposite

In 250 mL beaker, 0.2 g of clay was mixed with 250 mL of double-distilled water until a uniform solution was obtained. Another 250 mL beaker was used to hold 0.2 g of ZnO during 30 min ultrasonication process. The solution was then thoroughly mixed in a 460 r/min, 90 °C refluxing round bottom flask (RB). After 3 h, the solution was allowed to settle at room temperature. It was then filtered using 25 mm Whatman filter paper, rinsed with ethanol, and heated in a hot air oven at 100 °C for 12 h. The solution is now ready for use. Clay/ZnO nanoparticles were synthesized, as depicted in Fig. 1.

3. Result and discussion

3.1. X-ray diffraction studies (XRD)

An X-ray diffractometer (Shimadzu-7000) with monochromatized CuKα radiation was used to characterize the powder's atomic structure and quantify its crystal size. Full width at half maximum (FWHM) measurements and analysis utilizing the Debye Scherrer's Eq. (1) was used to determine the particle sizes.

$$D = \frac{0.9\lambda}{\beta\cos\theta}, \tag{1}$$

where D is constant related to the shape of the crystalline domains (typically around 0.9), λ is wavelength of the X-ray radiation used (in this case, CuKα radiation), β is full width at half maximum (FWHM) of the diffraction peak and θ is diffraction angle at which the peak is observed.

Fig. 2 displays the average crystallite sizes of the clay (38.37 nm), ZnO (36.39 nm), and clay/ZnO nanocomposite (33.46 nm). The X-ray

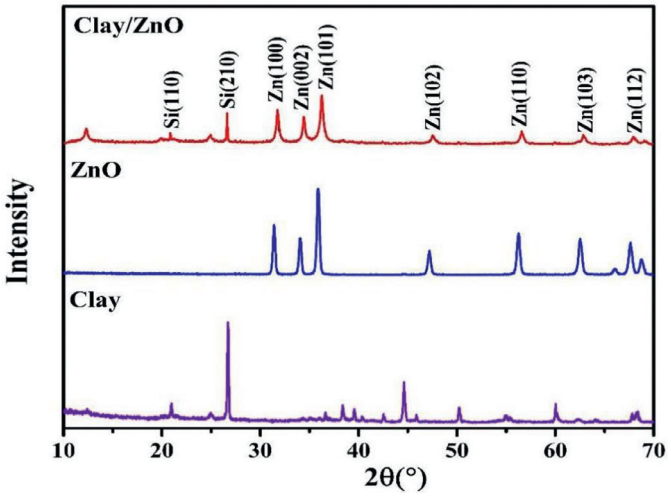

Fig. 2. XRD spectrum of clay, ZnO, and clay/ZnO.

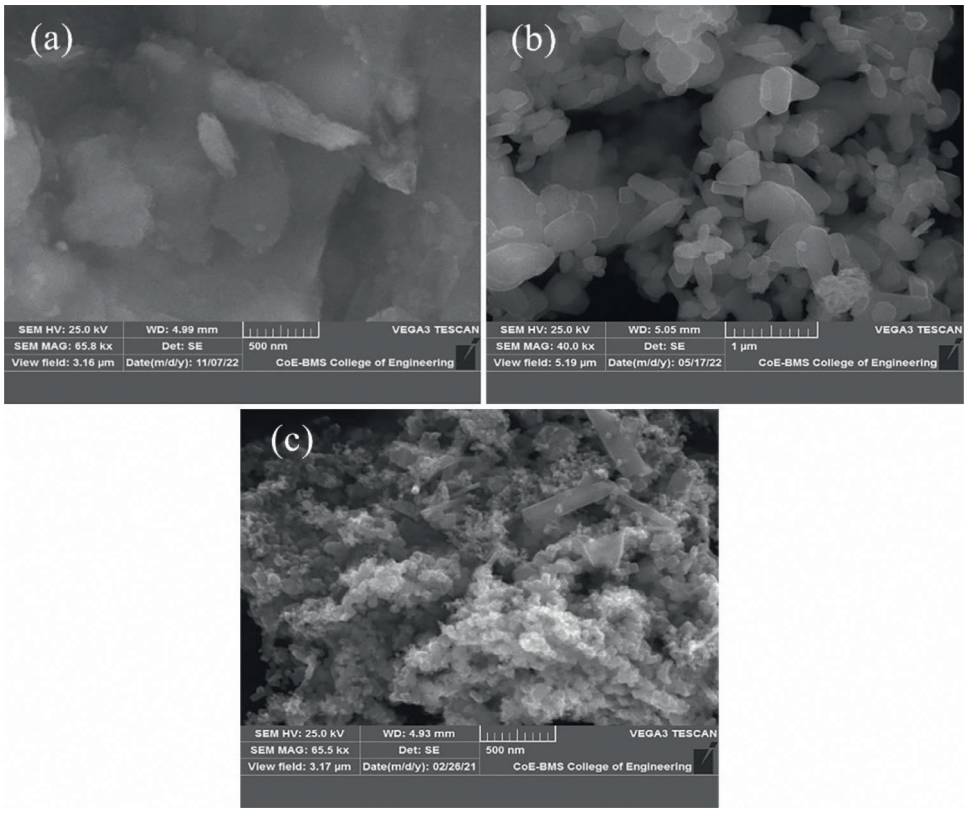

Fig. 3. SEM image of (a) clay, (b) ZnO, and (c) clay/ZnO.

Table 1
Chemicals used in the experiment (analytical grade without any further purification or modification).

Materials	Formula	Specification	Suppliers
Zinc nitrate	$Zn(NO_3)_2$	189.36 g/mol	Merck, Bengaluru
Urea	NH_2CONH_2	60.06 g/mol	Merck, Bengaluru
Clay	$Al_2O_3{\cdot}2SiO_2{\cdot}2H_2O$	–	Karnataka

diffraction (XRD) patterns, clearly exhibited clearer and stronger peaks for clay, ZnO, and the clay/ZnO nanocomposites, indicating their high crystallinity.

3.2. Scanning electron microscopy (SEM)

The synthesized particle was examined using a scanning electron microscope (SEM) on a Tescan Vega 3 device. Fig. 3 shows scanning electron micrographs of clay, ZnO, and clay/ZnO. Clay has a flattened or platy form, as seen in Fig. 3(a), with an average size on the order of 1 µm. ZnO, shown in Fig. 3(b), has a flake-like shape due to the aggregation of its nanoparticles into larger linked structures without clear boundaries. ZnO particles display a variety of geometric forms, including cubic, hexagonal, rhombic, and others, while clay particles retain their platy shape. The synthesized clay/ZnO nanocomposite (Fig. 3(c)) exhibits a uniform particle distribution. In contrast to the ZnO particles, which have rough surfaces and intertwine to form complex geometries, the clay particles have retained their flat shape (Table 1).

3.3. Energy dispersive X-ray analysis (EDAX)

The Tescan Vega 3 equipment was used to characterize the synthesized particles using EDAX analysis. Fig. 4 displays the results of the EDAX investigation of clay, ZnO, and the clay/ZnO nanoparticles. In Fig. 4(a), the components of clay, including silica, carbon, oxygen, iron, and aluminum, can be seen as revealed by the EDAX analysis, providing insight into the compound's composition. The EDAX results for ZnO, manufactured using the solution combustion technique with urea as the fuel, are shown in Fig. 4(b). The examination reveals a high weight percentage of Zinc (Zn) and oxygen (O), indicating that they constitute the major constituents of ZnO. The EDAX results for the reflux-made clay/ZnO nanocomposite are shown in Fig. 4(c). The results show a high concentration of zinc, as well as oxygen, carbon, silica, aluminum, sodium, and other elements in trace levels. This indicates the presence of these components in the clay/ZnO nanocomposite, although in low concentrations. Table 2 provides a list of the various elements present.

Table 2
EDAX analysis of clay, ZnO, and clay/ZnO (%).

Elements Sample	Sample		
	clay	ZnO	clay/ZnO
C	12.42	–	3.10
O	50.57	6.92	52.55
Na	0.16	–	0.02
Mg	–	–	0.71
Al	13.86	–	17.62
Si	16.04	–	21.78
K	0.60	–	1.11
Ca	0.31	–	0.01
Fe	6.04	–	2.70
Zn	–	93.08	0.41

4. Electrochemical and sensor studies

To fabricate the working electrodes, 0.025 g of the active material was combined with 0.475 g of graphite and then bound with 3–5 drops of polytetrafluoroethylene (PTFE) solution. An Ag/AgCl electrode

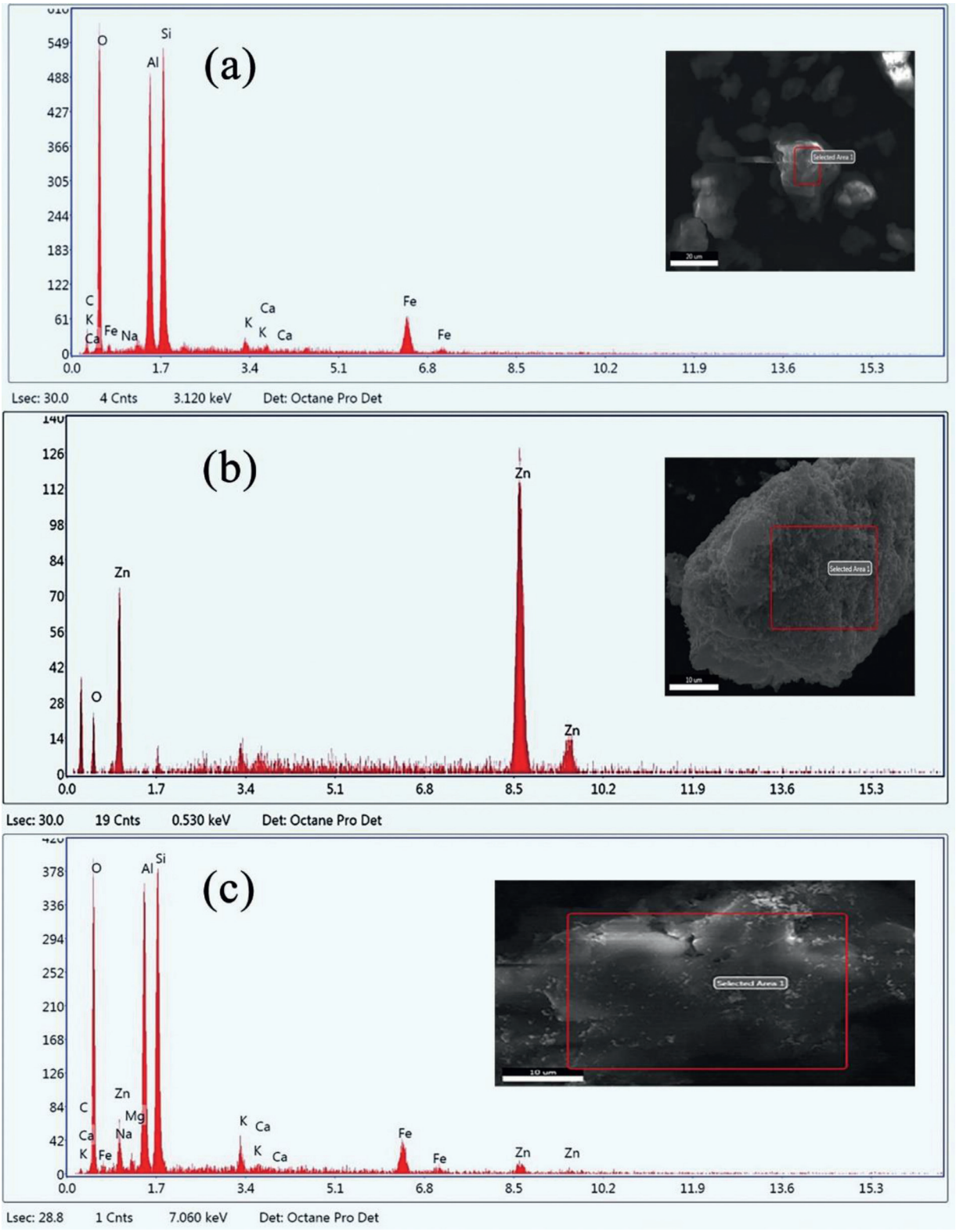

Fig. 4. EDAX spectrum of (a) clay, (b) ZnO, and (c) clay/ZnO.

served as the reference electrode, whereas a platinum counter electrode completed the electrochemical setup. Both clay and clay/ZnO electrodes were used in this arrangement. It was found that the clay/ZnO electrode had a decreased reversibility of the reaction compared to the clay electrode, as shown in Tables 3 and 4. Both electrodes exhibited quasi-reversible electron transfer in their cyclic voltammetry (CV) curves. These findings demonstrate that the redox process is crucial for the capacitive behavior of the electrodes. Eq. (2) is the Randles–Sevcik equation for calculating the height current in reversible processes.

$$I_p = 2.69 \times 105 \times n^{\frac{3}{2}} \times A \times D^{\frac{1}{2}} \times C_0 \times \upsilon^{\frac{1}{2}}, \quad (2)$$

Table 3
Electrochemical reversibility, diffusion coefficient and capacitance value of clay.

Scan rate /(mV s^{-1})	E_O/(10^{-5} V)	E_R/(10^{-5} V)	E_O–E_R /(10^{-5} V)	D/cm^2	Capacitance /(F g^{-1})
10	1.650	9.052	0.745		
20	1.930	8.341	1.096		
30	2.008	6.921	1.316	1.327×10^{-6}	105.3
40	2.097	6.560	1.441		
50	2.239	6.038	1.636		
60	2.270	4.960	1.774		

Table 4
Electrochemical reversibility, diffusion coefficient, and capacitance value of clay/ZnO.

Scan rate /(mV s^{-1})	E_O/(10^{-5} V)	E_R/(10^{-5} V)	E_O–E_R/(10^{-5} V)	D/cm^2	Capacitance /(F g^{-1})
10	2.185	9.269	1.259		
20	2.336	5.122	1.259		
30	2.449	1.353	2.314	1.341×10^{-6}	164.47
40	2.637	−5.310	7.940		
50	2.710	−6.560	9.240		
60	2.788	−9.956	12.730		

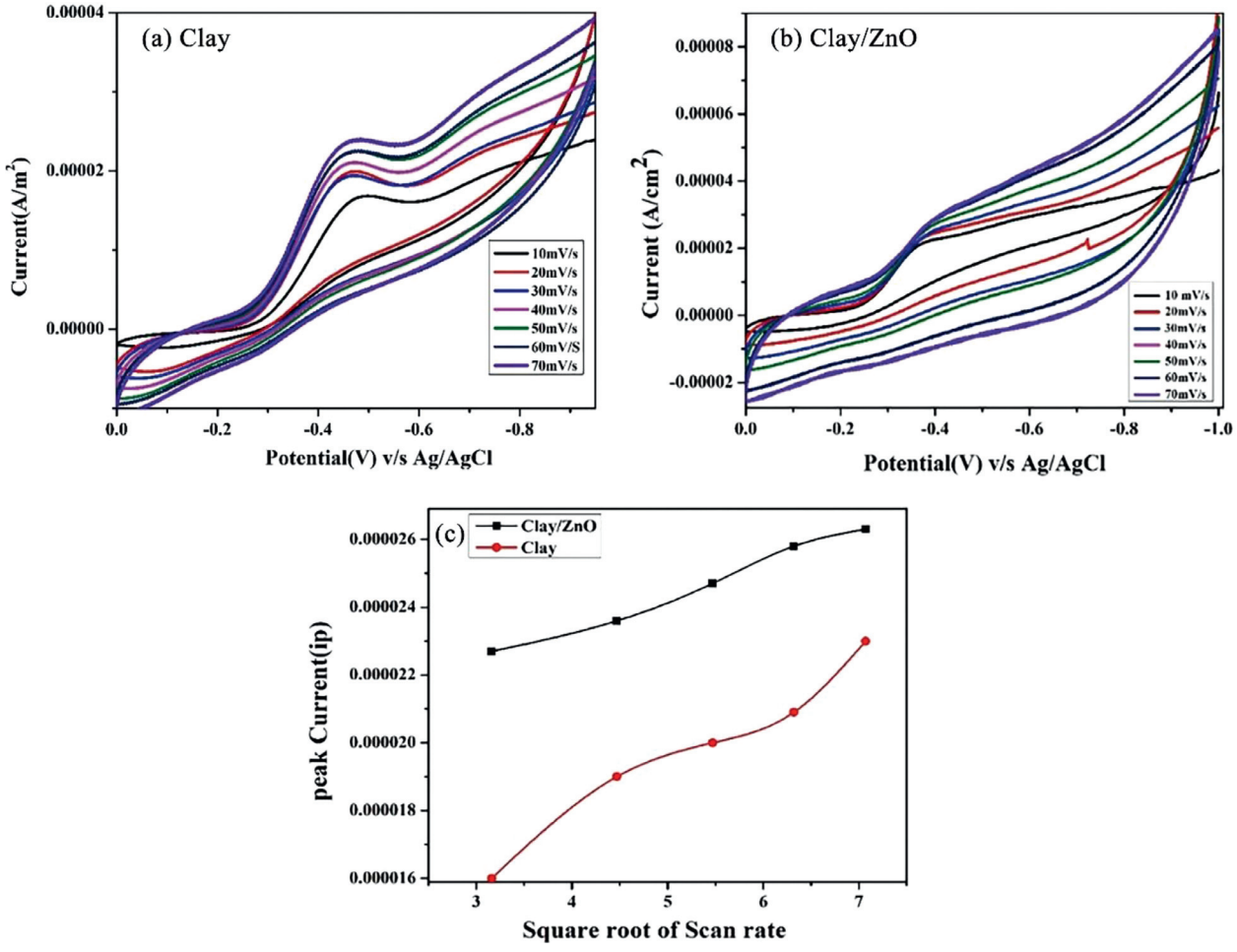

Fig. 5. CV curves of (a) clay, (b) clay/ZnO, and (c) diffusion coefficient of (clay, clay/ZnO).

where n is the total number of electrons involved in the redox process, A is total area of the active surface of the electrode, D is diffusion coefficient of the electroactive species, v is the scanning rate in the CV experiment, and C_0 is initial concentration of the electroactive material in the solution.

CV was used to test the electrochemical characteristics of the clay and clay/ZnO nanocomposite in 0.1 M KOH solution. As shown in Figs. 5(a)(b), the potential scan rate varied from 0.0 to 1.0 V. The capacitances of the clay and clay/ZnO nanocomposite electrodes were calculated using CV analysis, and the results are shown in Tables 3 and 4. The results showed that the clay electrode had a capacitance of 105.3 F g^{-1}, whereas the clay/ZnO nanocomposite electrode had a capacitance of 164.47 F g^{-1}. The proton diffusion coefficient (D) was used to evaluate the electrode reactions of both clay and clay/ZnO owing to the linear

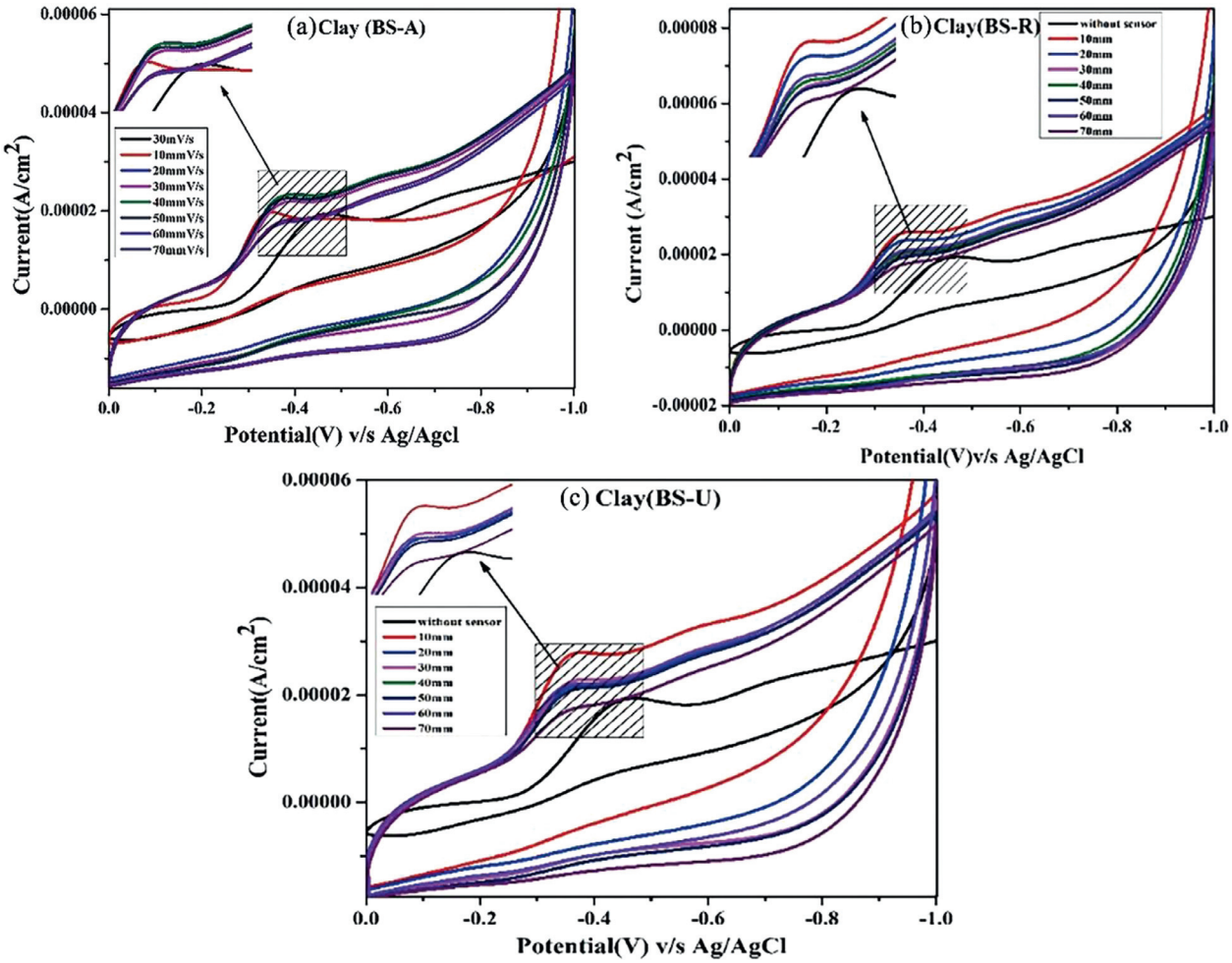

Fig. 6. Clay sensor studies in 0.1 M KOH of (a) BS-A, (b) BS-R, and (c) BS-U.

connection between the peak current (*ip*) and square root of the number of electrons transported ($n1/2$). Fig. 5(c) shows that the *D* value for clay/ZnO is greater than that of clay, suggesting that the electrochemical activity of the clay/ZnO nanocomposite is more effective than that of clay.

The chemical sensing capabilities of clay and clay/ZnO nanocomposite electrodes were investigated using cyclic voltammetry in the potential range of 0.00 to −1.00 V (Figs. 6(a)–(c) and 7(a)–(c)). These graphs show how the reduction and oxidation peak potentials shift as the concentration increases from 1 to 5 mM in an alkaline medium, indicating the potential of this technology for use in real-world sensing applications. Significant differences in the anodic oxidation peak potentials were observed when the synthesized materials were tested for ascorbic acid (BS-A), resorcinol (BS-R), and uric acid (BS-U). The peak potential variation was +0.22 V at the clay electrode and −0.44 V at the clay/ZnO nanocomposite electrode. Various shifts revealed the reactivity of the electrodes toward various substances. The observed shifts in the oxidation and reduction peaks support the efficacy of nickel-mesh graphite electrodes for sensing activities, further emphasizing their potential for chemical sensing applications.

Bio-sensing (BS) detection of ascorbic acid (BS-A), resorcinol (BS-R), and uric acid (BS-U) in a 0.1 M KOH electrolyte is shown in Fig. 6 as CV responses. Ascorbic acid detection by a biosensor is shown in Fig. 6(a) for an oxidative potential range of −0.30 to −0.50 V. V for the biosensor-based range of −0.26 to −0.37 V is depicted in Fig. 6(b). As shown in Fig. 6(c), the biosensor is sensitive to uric acid in the oxidative potential range of −0.24 to −0.42 V. In 0.1 M KOH on a clay nickel mesh electrode, resorcinol had the highest detection efficiency of the three biosensors tested.

Fig. 7 displays the CV responses from the biosensing (BS) of ascorbic acid (BS-A), resorcinol (BS-R), and uric acid (BS-U) in a 0.1 M KOH electrolyte. The biosensor was able to pick up on ascorbic acid at oxidative potentials between −0.21 and −0.52 V (Fig. 7(a)). For resorcinol bio-sensor detection, the oxidative potential range is demonstrated in Fig. 7(b) to be between −0.33 and −0.39 V. In Fig. 7(c), we see a biosensor detect uric acid throughout an oxidative potential range of −0.32 to −0.55 V. Among the three bio-sensors tested in 0.1 M KOH, uric acid is the easiest to detect using a clay/ZnO nickel mesh electrode.

5. Photocatalytic studies

As shown in Fig. 8, the generated nanocomposite underwent the photocatalytic degradation of malachite green dye when exposed to UV–visible (UV–vis) light. A UV–vis spectrophotometer was used to monitor the adsorption by periodically pipetting 5 mL of the dye solution. The concentration of the malachite green dye was determined by measuring its absorbance at 624 nm. Eq. (3) was used to calculate the reduction efficiency.

$$\text{Degradation efficiency} = \frac{C_i - C_f}{C_i} \times 100\%, \tag{3}$$

where C_i is the initial concentration, and C_f is the reaction concentration of the malachite green dye before and after irradiation.

Finally, the absorbance was measured at 624 nm to evaluate the dye swatches. For the malachite green dye (20×10^{-6} for 90 min), the photo-

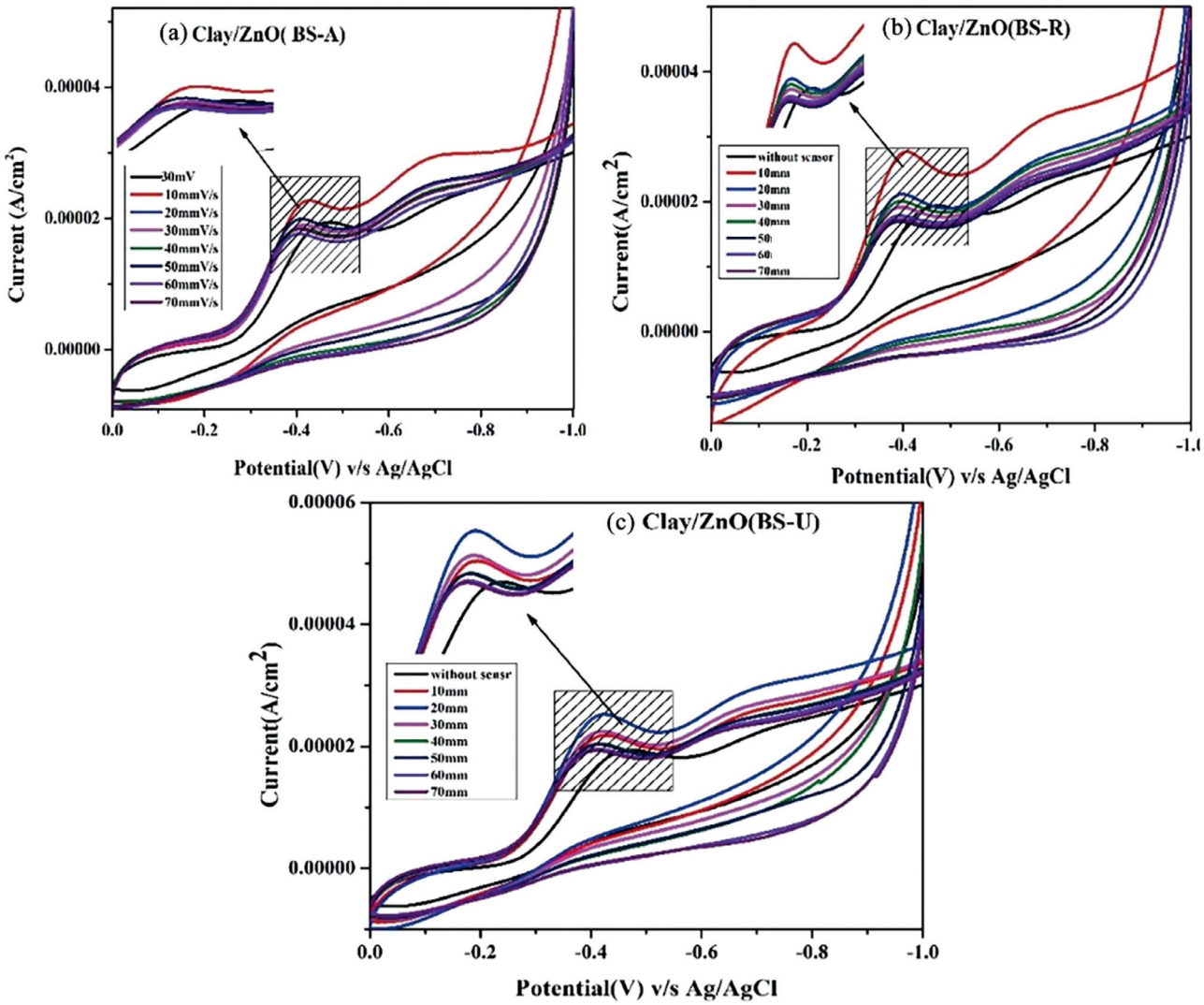

Fig. 7. Clay/ZnO sensor studies in 0.1 M KOH of (a) BS-A, (b) BS-R, and (c) BS-U.

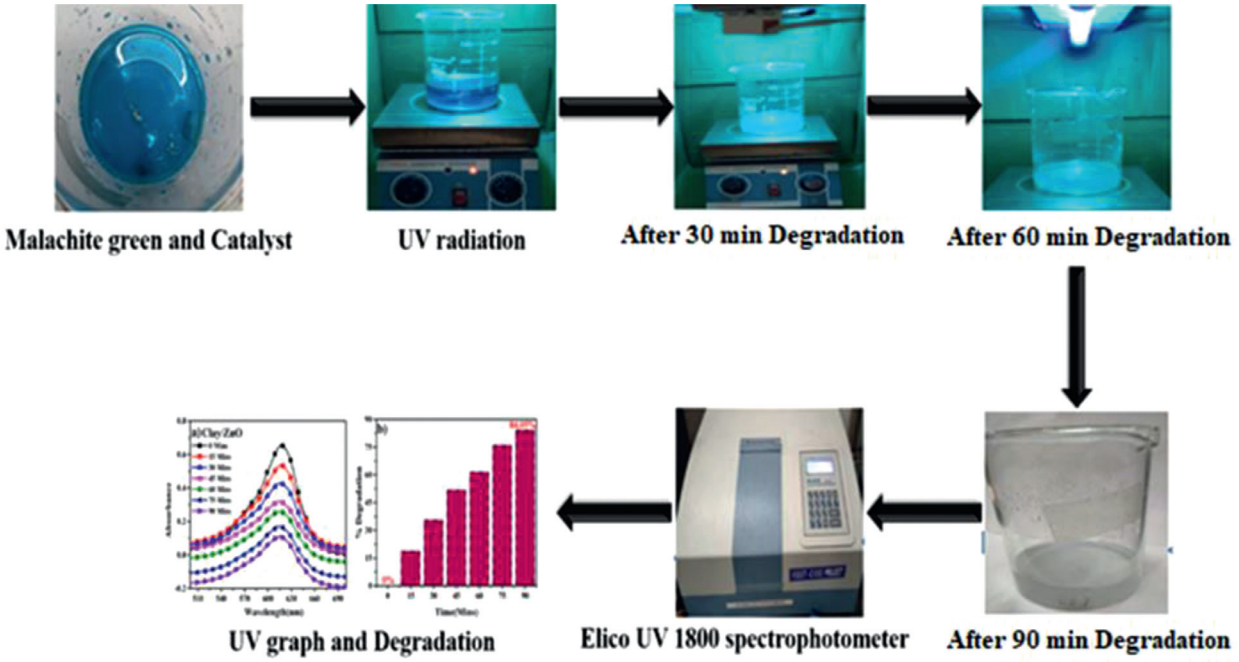

Fig. 8. Flowchart for photocatalytic activity of clay and clay/ZnO.

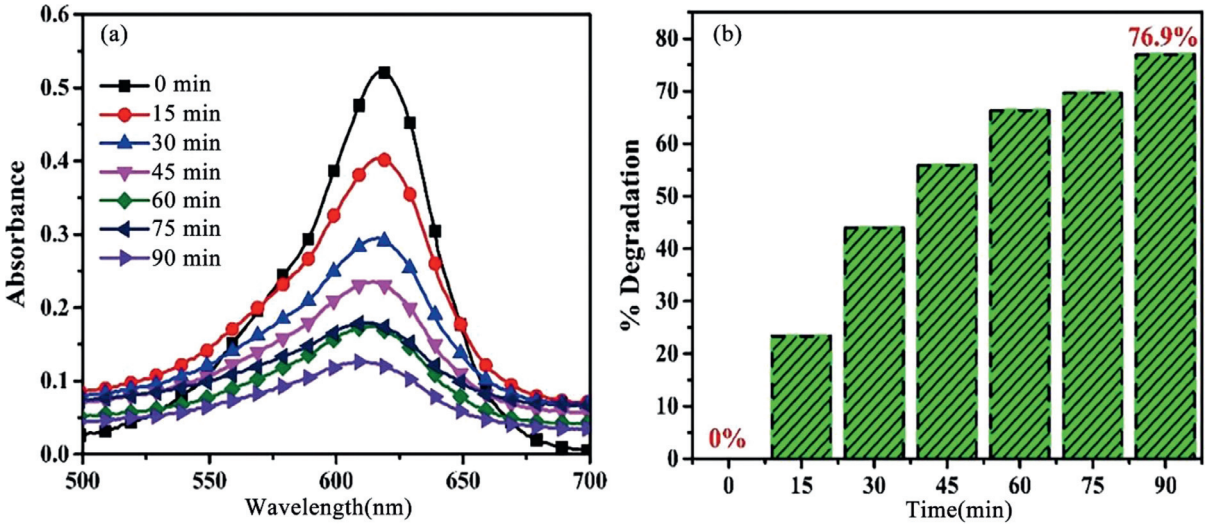

Fig. 9. (a) UV graph and (b) degradation(%) of malachite green using clay catalyst.

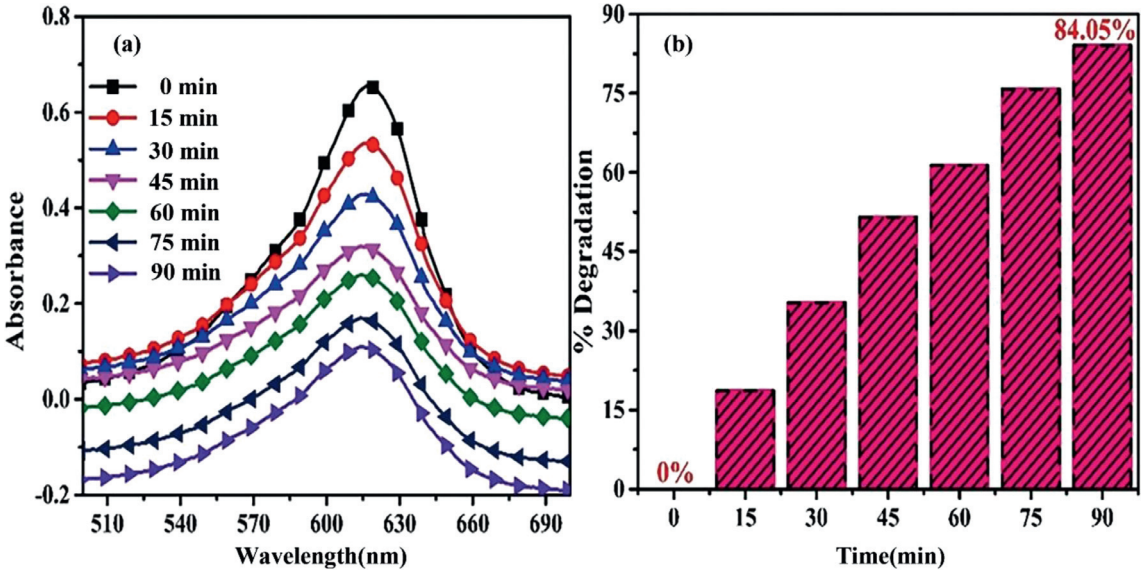

Fig. 10. (a) UV graph and (b) degradation(%) of malachite green using clay/ZnO catalyst.

Table 5
Photocatalytic degradation of malachite green using clay.

Time/min	Absorbance	Concentration/ $\times 10^{-6}$	Degradation/%
0	0.523	20.00	0.00
15	0.401	15.33	23.35
30	0.293	11.20	44.00
45	0.231	8.83	55.85
60	0.176	6.73	66.35
75	0.159	6.08	69.60
90	0.121	4.62	76.90

Table 6
Photocatalytic degradation of malachite green using clay/ZnO.

Time/min	Absorbance	Concentration/ $\times 10^{-6}$	Degradation/%
0	0.657	20.00	0.00
15	0.535	16.28	18.60
30	0.425	12.93	35.35
45	0.318	9.68	51.60
60	0.254	7.73	61.35
75	0.160	4.87	75.85
90	0.105	3.19	84.05

catalytic activity of the clay/ZnO nanocomposite was 84.05%, whereas that of the clay nanoparticles was only 76.9% (Figs. 9 and 10; Tables 5 and 6). It has been shown that the photodegradation activities of photocatalysts are profoundly affected by the particle size, shape, and surface features of the materials. The combination of a low recombination rate and robust interfacial charge transfer is responsible for the enhanced photocatalytic efficiency observed upon decreasing the crystal size. In addition to producing superoxide radicals (O_2•) through electron activity, VB holes react with water to generate hydroxyl radicals (OH•) [41–45].

6. Antioxidant activities

The DPPH assay (Fig. 11) was used to evaluate the antioxidant activities of the clay and clay/ZnO nanoparticles at 517 nm. Each of the five labelled test tubes contained a different volume of solution (rang-

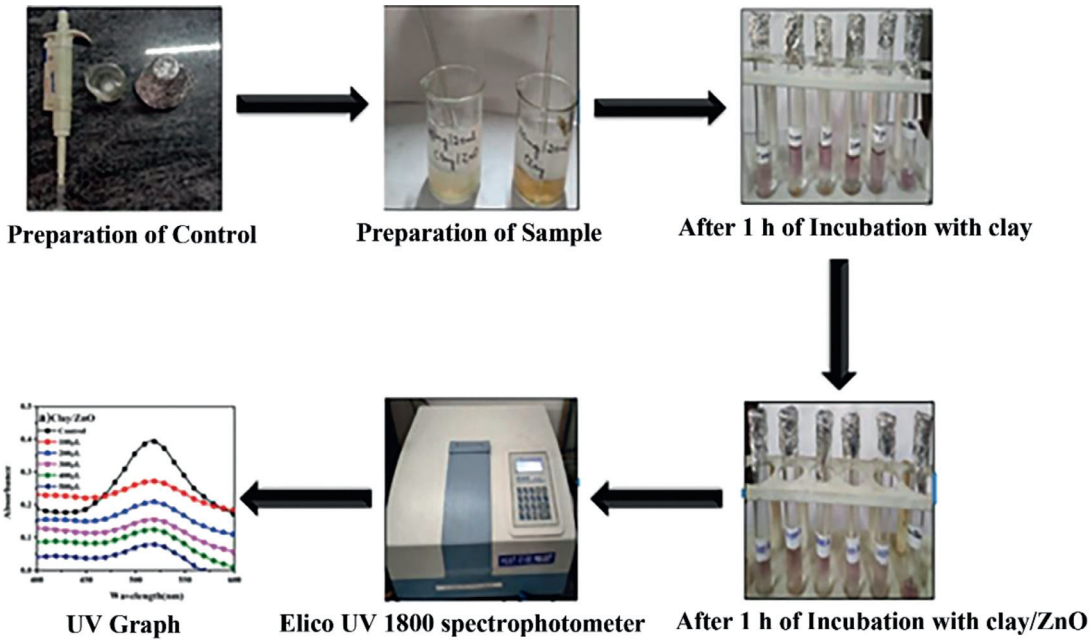

Fig. 11. Flowchart for the antioxidant activity of clay and clay/ZnO.

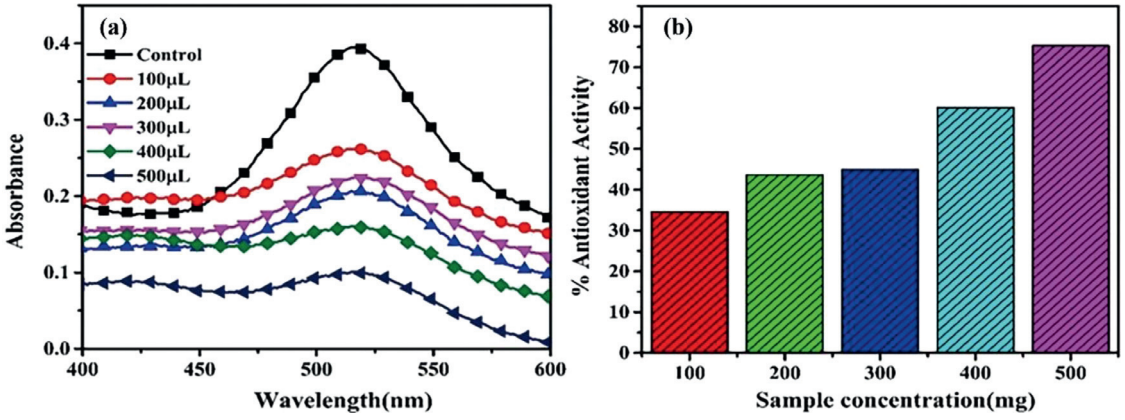

Fig. 12. (a) UV absorption spectrum and (b) antioxidant activity of clay.

Table 7
Antioxidant activity of clay.

Volume of sample/mL	Volume of methanol/mL	Concentration/μg	Absorbance	Activity/%	IC-50/(mg mL^{-1})
100	500	1000	0.259	34.59	
200	400	2000	0.223	43.68	
300	300	3000	0.203	44.98	282.517
400	200	4000	0.158	60.10	
500	100	5000	0.098	75.25	
Control	600	–	0.396	–	

ing from 100 to 500 mL). Methanol was added to each test tube via a micropipette. Each test tube contained 2 mL of newly prepared DPPH solution, and then the tubes were wrapped in aluminum foil and stored in the dark for approximately an hour. The absorbance of the solution was measured using a UV–vis spectrophotometer (Elico UV 1800 spectrophotometer) [46]. Therefore, the proportion of antioxidant properties was determined using Eq. (4).

$$\text{Antioxidant activity} = \frac{A_C - A_S}{A_C} \times 100\%, \quad (4)$$

where A_c is absorbance of the control and A_s is absorbance of the sample.

The UV absorption spectra and antioxidant properties of the clay and clay/ZnO nanoparticles are shown in Figs. 12(a)(b) and 13(a)(b), respectively. The antioxidant activity estimation and IC50 value calculation methods are presented in Tables 7 and 8, respectively. The clay and clay/ZnO nanoparticles exhibited radical-scavenging activities of 282.517 and 236.493 mg/mL, respectively. The IC50 value for neutralizing free radicals should be set at the maximum possible degree of antioxidant activity [47]. Clay and clay/ZnO NPs can scavenge DPPH free radicals by transferring an electron to an oxygen atom to create stable DPPH molecules. When added to methanolic DPPH solutions at varying concentrations, the pink hue of the unstable DPPH solution disappeared.

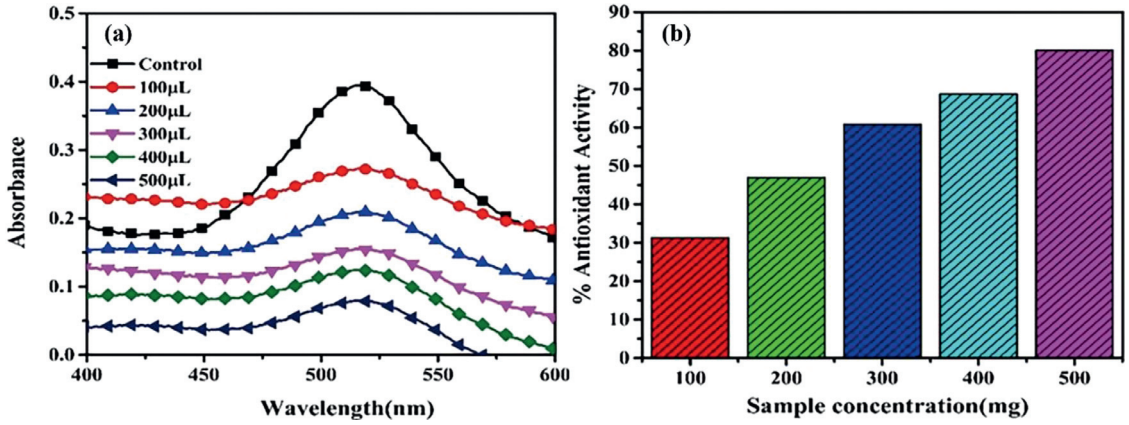

Fig. 13. (a) UV absorption spectrum and (b) antioxidant activity of clay/ZnO.

Table 8
Antioxidant activity of clay/ZnO.

Volume of sample/mL	Volume of methanol/mL	Concentration/μg	Absorbance	Activity/%	IC-50/(mg mL^{-1})
100	500	1000	0.272	31.31	
200	400	2000	0.215	46.96	
300	300	3000	0.155	60.85	236.493
400	200	4000	0.124	68.68	
500	100	5000	0.079	80.05	
Control	600	–	0.396	–	

7. Conclusion

Based on these findings, we employed a chemical method to develop and test a low-cost hybrid nano adsorbent composed of clay/ZnO.

(1) The X-ray diffraction (XRD) patterns confirmed the clay/ZnO, spinel, or cubic structure. Clay was found to be evenly distributed throughout the composite, as determined by the FESEM investigation of the composition of the material.
(2) The larger potential reversibility disparity of −0.6 to 0.6 V was seen in the clay/ZnO CV investigation. Clay/ZnO-carbon paste electrodes exhibited considerable shifts in the oxidation and reduction peaks, proving the use of this material in sensor applications.
(3) CV measurements of clay/ZnO were enhanced to detect heavy metals using sensors for biomolecules (dextrose), eye-drop chemicals, and stannous chloride.

Based on these results, it is likely that the synthesized clay/ZnO could be used in a wide range of applications, including chemical and biosensors for electrochemical sensing, heavy metal analysis, and commercial wastewater treatment.

Declaration of Competing Interest

The authors declare no competing Interests.

References

[1] S.H. Tamboli, R.B. Patil, S.V. Kamat, V. Puri, R.K. Puri, Modification of optical properties of MgO thin films by vapour chopping, J. Alloy. Compd. 477 (2009) 855–859, doi:10.1016/j.jallcom.2008.11.011.
[2] A Lempicki, The electrical conductivity of MgO single crystals at high temperatures, Proc. Phys. Soc. B 66 (1953) 281–283, doi:10.1088/0370-1301/66/4/304.
[3] A. Kalam, A.G. Al-Sehemi, M. Assiri, G. Du, T. Ahmad, I. Ahmad, M. Pannipara, Modified solvothermal synthesis of cobalt ferrite ($CoFe_2O_4$) magnetic nanoparticles photocatalysts for degradation of methylene blue with H_2O_2/visible light, Results Phys. 8 (2018) 1046–1053, doi:10.1016/j.rinp.2018.01.045.
[4] Á.D.J. Ruíz-Baltazar, S.Y. Reyes-López, M.D.L. Mondragón-Sánchez, A.I. Robles-Cortés, R. Pérez, Eco-friendly synthesis of Fe_3O_4 nanoparticles: Evaluation of their catalytic activity in methylene blue degradation by kinetic adsorption models, Results Phys. 12 (2019) 989–995, doi:10.1016/j.rinp.2018.12.037.
[5] M. Mylarappa, N. Raghavendra, B.S. Surendra, K.N. Shravana Kumar, S. Kantharjau, Electrochemical, photocatalytic and sensor studies of clay/MgO nanoparticles, Appl. Surf. Sci. Adv. 10 (2022) 100268, doi:10.1016/j.apsadv.2022.100268.
[6] H.A. Wahab, A.A. Salama, A.A. El-Saeid, O. Nur, M. Willander, I.K. Battisha, Optical, structural and morphological studies of (ZnO) nano-rod thin films for biosensor applications using sol gel technique, Results Phys. 3 (2013) 46–51, doi:10.1016/j.rinp.2013.01.005.
[7] B.W. Liu, C.B. Bie, Y. Zhang, L.X. Wang, Y.J. Li, J.G. Yu, Hierarchically porous ZnO/g-C_3N_4 S-scheme heterojunction photocatalyst for efficient H_2O_2 production, Langmuir 37 (2021) 14114–14124, doi:10.1021/acs.langmuir.1c02360.
[8] W.L. Yu, J.F. Zhang, T.Y. Peng, New insight into the enhanced photocatalytic activity of N-, C- and S-doped ZnO photocatalysts, Appl. Catal. B: Environ. 181 (2016) 220–227, doi:10.1016/j.apcatb.2015.07.031.
[9] N. Raghavendra, H.N. Narasimha Murthy, M. Krishna, K.R. Vishnu Mahesh, R. Sridhar, S. Firdosh, G. Angadi, S.C. Sharma, Mechanical behavior of organo-modified Indian bentonite nanoclay fiber-reinforced plastic nanocomposites, Front. Mater. Sci. 7 (2013) 396–404, doi:10.1007/s11706-013-0224-6.
[10] C.V. Moolya, N.P. Shetti, D.S. Nayak, Clay coated carbon electrode sensor for a food dye sunset yellow, Mater. Today: Proc. 18 (2019) 1116–1123, doi:10.1016/j.matpr.2019.06.571.
[11] N. Raghavendra, H.N. Narasimha Murthy, S. Firdosh, R. Sridhar, G. Angadi, K.R. Vishnu Mahesh, M. Krishna, Moisture diffusion through (hexadecyltrimethylammonium bromide - Indian bentonite)/(vinylester) nanocomposites in artificial seawater and demineralized water, J. Vinyl. Addit. Technol. 22 (2016) 441–451, doi:10.1002/vnl.21463.
[12] N. Raghavendra, H.N. Murthy, S. Firdosh, R. Sridhar, G. Angadi, K.V. Mahesh, M. Krishna, Combined influence of organo-modified Indian bentonite nanoclay and fire retardants on thermal and fire behavior of vinylester, Proc. Inst. Mech. Eng., Part N: J. Nanomater., Nanoeng. Nanosyst. 231 (2017) 34–42, doi:10.1177/1740349916635205.
[13] N. Raghavendra, H.N. Narasimha Murthy, K.R. Vishnu Mahesh, M. Mylarappa, D.M. K.Siddeswara, M. Krishna, Influence of nanoclays to the matrix of vinylester/glass composites on their fire behavior properties, Mater. Today: Proc. 5 (2018) 22526–22535, doi:10.1016/j.matpr.2018.06.624.
[14] N. Raghavendra, H.N.N. Murthy, K.R.V. Mahesh, M. Mylarappa, K.P. Ashik, D.M.K. Siddeswara, M. Krishna, Effect of nanoclays on the performance of mechanical, thermal and flammability of vinylester based nanocomposites, Mater. Today: Proc. 4 (2017) 12109–12117, doi:10.1016/j.matpr.2017.09.138.
[15] M.A. Barakat, New trends in removing heavy metals from industrial wastewater, Arab. J. Chem. 4 (2011) 361–377, doi:10.1016/j.arabjc.2010.07.019.
[16] C.R. Ravi Kumar, M.S. Santosh, H.P. Nagaswarupa, S.C. Prashantha, S. Yallappa, M.R. Anil Kumar, Synthesis and characterization of β-$Ni(OH)_2$ embedded with MgO and ZnO nanoparticles as nanohybrids for energy storage devices, Mater. Res. Express 4 (2017) 065503, doi:10.1088/2053-1591/aa73a5.
[17] G. Suresh Kumar, J. Akbar, R. Govindan, E.K. Girija, M. Kanagaraj, A novel rhombohedron-like nickel ferrite nanostructure: Microwave combustion synthesis, structural characterization and magnetic properties, J. Sci.: Adv. Mater. Devices 1 (2016) 282–285, doi:10.1016/j.jsamd.2016.07.003.

[18] P.R. Vernekar, N.P. Shetti, M.M. Shanbhag, S.J. Malode, R.S. Malladi, K.R. Reddy, Novel layered structured bentonite clay-based electrodes for electrochemical sensor applications, Microchem. J. 159 (2020) 105441, doi:10.1016/j.microc.2020.105441.
[19] M. Kaur, M. Singh, S.S. Mukhopadhyay, D. Singh, M. Gupta, Structural, magnetic and adsorptive properties of clay ferrite nanocomposite and its use for effective removal of Cr(VI) from water, J. Alloy. Compd. 653 (2015) 202–211, doi:10.1016/j.jallcom.2015.08.265.
[20] N.P. Shetti, S.J. Malode, D.S. Nayak, R.R. Naik, G.T. Kuchinad, K.R. Reddy, S.S. Shukla, T.M. Aminabhavi, Hetero-nanostructured iron oxide and bentonite clay composite assembly for the determination of an antiviral drug acyclovir, Microchem. J. 155 (2020) 104727, doi:10.1016/j.microc.2020.104727.
[21] B. Shruthi, B.J. Madhu, V.B. Raju, S. Vynatheya, B.V. Devi, G.V. Jayashree, C.R. Ravikumar, Synthesis, spectroscopic analysis and electrochemical performance of modified β-nickel hydroxide electrode with CuO, J. Sci.: Adv. Mater. Devices 2 (2017) 93–98, doi:10.1016/j.jsamd.2016.12.002.
[22] V. Srivastava, Y.C. Sharma, M. Sillanpää, Application of nano-magnesso ferrite (n-$MgFe_2O_4$) for the removal of Co^{2+} ions from synthetic wastewater: Kinetic, equilibrium and thermodynamic studies, Appl. Surf. Sci. 338 (2015) 42–54, doi:10.1016/j.apsusc.2015.02.072.
[23] M. Kaur, N. Kaur, K. Jeet, P. Kaur, $MgFe_2O_4$ nanoparticles loaded on activated charcoal for effective removal of Cr(VI)–A novel approach, Ceram. Int. 41 (2015) 13739–13750, doi:10.1016/j.ceramint.2015.08.040.
[24] N. Sivakumar, S.R.P. Gnanakan, K. Karthikeyan, S. Amaresh, W.S. Yoon, G.J. Park, Y.S. Lee, ChemInform abstract: Nanostructured $MgFe_2O_4$ as anode materials for lithium-ion batteries, ChemInform 42 (2011), doi:10.1002/chin.201132006.
[25] S. Kanagesan, M. Hashim, S. Tamilselvan, N.B. Alitheen, I. Ismail, G. Bahmanrokh, Cytotoxic effect of nanocrystalline $MgFe_2O_4$ particles for cancer cure, J. Nanomater. 2013 (2013) 1–8, doi:10.1155/2013/865024.
[26] J. Patil, D. Nadargi, I.S. Mulla, S.S. Suryavanshi, Spinel $MgFe_2O_4$ thick films: A colloidal approach for developing gas sensors, Mater. Lett. 213 (2018) 27–30, doi:10.1016/j.matlet.2017.11.009.
[27] Y. Zu, Y. Zhao, K. Xu, Y. Tong, F. Zhao, Preparation and comparison of catalytic performance for nano $MgFe_2O_4$, GO-loaded $MgFe_2O_4$ and GO-coated $MgFe_2O_4$ nanocomposites, Ceram. Int. 42 (2016) 18844–18850, doi:10.1016/j.ceramint.2016.09.030.
[28] M.M. Rashad, Magnetic properties of nanocrystalline magnesium ferrite by co-precipitation assisted with ultrasound irradiation, J. Mater. Sci. 42 (2007) 5248–5255, doi:10.1007/s10853-006-0389-9.
[29] S. Ilhan, S.G. Izotova, A.A. Komlev, Synthesis and characterization of $MgFe_2O_4$ nanoparticles prepared by hydrothermal decomposition of co-precipitated magnesium and iron hydroxides, Ceram. Int. 41 (2015) 577–585, doi:10.1016/j.ceramint.2014.08.106.
[30] S. Akbari, S.M. Masoudpanah, S.M. Mirkazemi, N. Aliyan, PVA assisted coprecipitation synthesis and characterization of $MgFe_2O_4$ nanoparticles, Ceram. Int. 43 (2017) 6263–6267, doi:10.1016/j.ceramint.2017.02.030.
[31] N. Raghavendra, H.P. Nagaswarupa, T.R.S. Shekhar, M. Mylarappa, B.S. Surendra, S.C. Prashantha, C.R. Ravikumar, M.R.A. Kumar, N. Basavaraju, Development of clay ferrite nanocomposite: Electrochemical, sensors and photocatalytic studies, Appl. Surf. Sci. Adv. 5 (2021) 100103, doi:10.1016/j.apsadv.2021.100103.
[32] A. Pradeep, P. Priyadharsini, G. Chandrasekaran, Sol–gel route of synthesis of nanoparticles of $MgFe_2O_4$ and XRD, FTIR and VSM study, J. Magn. Magn. Mater. 320 (2008) 2774–2779, doi:10.1016/j.jmmm.2008.06.012.
[33] M. Goodarz Naseri, M.H.M. Ara, E.B. Saion, A.H. Shaari, Superparamagnetic magnesium ferrite nanoparticles fabricated by a simple, thermal-treatment method, J. Magn. Magn. Mater. 350 (2014) 141–147, doi:10.1016/j.jmmm.2013.08.032.
[34] Y. Feng, S. Li, Y. Zheng, Z. Yi, Y. He, Y. Xu, Preparation and characterization of $MgFe_2O_4$ nanocrystallites via PVA sol-gel route, J. Alloy. Compd. 699 (2017) 521–525, doi:10.1016/j.jallcom.2016.12.432.
[35] T. Sasaki, S. Ohara, T. Naka, J. Vejpravova, V. Sechovsky, M. Umetsu, S. Takami, B. Jeyadevan, T. Adschiri, Continuous synthesis of fine $MgFe_2O_4$ nanoparticles by supercritical hydrothermal reaction, J. Supercrit. Fluid 53 (2010) 92–94, doi:10.1016/j.supflu.2009.11.005.
[36] B.S. Randhawa, H. Kaur, H.S. Dosanjh, J. Singh, Precursor route for the synthesis of $MgFe_2O_4$ nanoparticles from the thermolysis of magnesium hexapropionatoferrate(III), Ceram. Int. 42 (2016) 8891–8894, doi:10.1016/j.ceramint.2016.02.142.
[37] N. Raghavendra, H.P. Nagaswarupa, T.R. Shashi Shekhar, M. Mylarappa, B.S. Surendra, S.C. Prashantha, N. Basavaraju, C.R. Ravi Kumar, M.R. Anil Kumar, Electrochemical sensor studies and optical analysis of developed clay based $CoFe_2O_4$ ferrite NPs, Sens. Int. 2 (2021) 100083, doi:10.1016/j.sintl.2021.100083.
[38] R. N, N.M. Hn, V.M. Kr, S. R, K M, Organomodification of Indian bentonite clay and its influence on fire behavior of nanoclay/vinylester composites, in: Proceedings of the Institution of Mechanical Engineers, Part N: Journal of Nanoengineering and Nanosystems, 229, 2015, pp. 55–65, doi:10.1177/1740349914520819.
[39] M.M. Rashad, M.G. El-Shaarawy, N.M. Shash, M.H. Maklad, F.A. Afifi, Controlling the composition, microstructure, electrical and magnetic properties of $LiFe_5O_8$ powders synthesized by sol gel auto-combustion method using urea as a fuel, J. Magn. Magn. Mater. 374 (2015) 495–501, doi:10.1016/j.jmmm.2014.08.090.
[40] A. Sugunan, C. Thanachayanont, J. Dutta, J.G. Hilborn, Heavy-metal ion sensors using chitosan-capped gold nanoparticles, Sci. Technol. Adv. Mater. 6 (2005) 335–340, doi:10.1016/j.stam.2005.03.007.
[41] M.A.S. Amulya, H.P. Nagaswarupa, M.R.A. Kumar, C.R. Ravikumar, K.B. Kusuma, Sonochemical synthesis of $MnFe_2O_4$ nanoparticles and their electrochemical and photocatalytic properties, J. Phys. Chem. Solids 148 (2021) 109661, doi:10.1016/j.jpcs.2020.109661.
[42] M. Mylarappa, V. Venkata Lakshmi, K.R. Vishnu Mahesh, H.P. Nagaswarupa, N. Raghavendra, Synthesis and characterization of Mn–$ZnFe_2O_4$ and Mn–$ZnFe_2O_4$ /rGO nanocomposites from waste batteries for photocatalytic, electrochemical and thermal studies, Mater. Res. Express 4 (2017) 115603, doi:10.1088/2053-1591/aa912f.
[43] S.D. Bukkitgar, N.P. Shetti, Fabrication of a TiO_2 and clay nanoparticle composite electrode as a sensor, Anal. Methods 9 (2017) 4387–4393, doi:10.1039/C7AY01068K.
[44] N.B. Arun Kumar, J. Sirajudeen, H.P. Nagaswarupa, C.R. Ravikumar, M.R. Anil Kumar, H.C. Ananda Murthy, Electrochemical and photocatalytic properties of green nickel oxide nanomaterial synthesized using plectranthus amboinicus plant leaf extract, Adv. Mater. Lett. 11 (2020) 1–6, doi:10.5185/amlett.2020.091559.
[45] N.P. Shetti, D.S. Nayak, G.T. Kuchinad, R.R. Naik, Electrochemical behavior of thiosalicylic acid at γ-Fe_2O_3 nanoparticles and clay composite carbon electrode, Electrochim. Acta 269 (2018) 204–211.
[46] M. Mylarappa, S. Chandruvasan, S. Kantharaju, S. Rekha, Synthesis and characterization of Rgo doped Nb_2O_5 nano composite for chemical sensor studies, ECS Trans. 107 (2022) 269–275, doi:10.1149/10701.0269ecst.
[47] J.F. Rivero-Cruz, J. Granados-Pineda, J. Pedraza-Chaverri, J.M. Pérez-Rojas, A. Kumar-Passari, G. Diaz-Ruiz, B.E. Rivero-Cruz, Phytochemical constituents, antioxidant, cytotoxic, and antimicrobial activities of the ethanolic extract of Mexican brown Propolis, Antioxidants 9 (2020) 70, doi:10.3390/antiox9010070.